PAPER

Image quality of list-mode proton imaging without front trackers

To cite this article: Jarle Rambo Sølie *et al* 2020 *Phys. Med. Biol.* **65** 135012

View the article online for updates and enhancements.

Recent citations

- A High-Granularity Digital Tracking Calorimeter Optimized for Proton CT
Johan Alme *et al*

Physics in Medicine & Biology

IPEM   Institute of Physics and Engineering in Medicine

Image quality of list-mode proton imaging without front trackers

Jarle Rambo Sølie[1,2,9] ⓘ, Lennart Volz[3,4,9] ⓘ, Helge Egil Seime Pettersen[5] ⓘ, Pierluigi Piersimoni[2] ⓘ, Odd Harald Odland[2,5], Dieter Röhrich[2], Håvard Helstrup[1] ⓘ, Thomas Peitzmann[6], Kjetil Ullaland[2], Monika Varga-Kofarago[7], Shruti Mehendale[2], Ola Slettevoll Grøttvik[2], Viljar Nilsen Eikeland[2], Ilker Meric[1,8] ⓘ and Joao Seco[3,4,8]

1   Department of Computer Science, Electrical Engineering and Mathematical Sciences, Western Norway University of Applied Sciences, 5020 Bergen, Norway
2   Department of Physics and Technology, University of Bergen, 5020 Bergen, Norway
3   Division Biomedical Physics in Radiation Oncology, German Cancer Research Center (DKFZ), 69120 Heidelberg, Germany
4   Department of Physics and Astronomy, Heidelberg University, 69120 Heidelberg, Germany
5   Department of Oncology and Medical Physics, Haukeland University Hospital, 5021 Bergen, Norway
6   Institute for Subatomic Physics, Utrecht University/Nikhef, Utrecht, Netherlands
7   Department for Theoretical Physics, Heavy-Ion Research Group, Wigner RCP of the Hungarian Academy of Sciences, 1121 Budapest, Hungary
8   These authors share senior authorship on this work.
9   These authors contributed equally to this work

E-mail: jars@hvl.no **and** l.volz@dkfz-heidelberg.de

Abstract

List mode proton imaging relies on accurate reconstruction of the proton most likely path (MLP) through the patient. This typically requires two sets of position sensitive detector systems, one upstream (front) and one downstream (rear) of the patient. However, for a clinical implementation it can be preferable to omit the front trackers (single-sided proton imaging). For such a system, the MLP can be computed from information available through the beam delivery system and the remaining rear tracker set. In this work, we use Monte Carlo simulations to compare a conventional double-sided (using both front and rear detector systems) with a single-sided system (only rear detector system) by evaluating the spatial resolution of proton radiographs (pRad) and proton CT images (pCT) acquired with these set-ups. Both the pencil beam spot size, as well as the spacing between spots was also adjusted to identify the impact of these beam parameters on the image quality.

Relying only on the pencil beam central position for computing the MLP resulted in severe image artifacts both in pRad and pCT. Using the recently extended-MLP formalism that incorporate pencil beam uncertainty removed these image artifacts. However, using a more focused pencil beam with this algorithm induced image artifacts when the spot spacing was the same as the beam spot size. The spatial resolution tested with a sharp edge gradient technique was reduced by 40% for single-sided ($MTF_{10\%} = 3.0$ lp/cm) compared to double-sided ($MTF_{10\%} = 4.9$ lp/cm) pRad with ideal tracking detectors. Using realistic trackers the difference decreased to 30%, with $MTF_{10\%}$ of 4.0 lp/cm for the realistic double-sided and 2.7 lp/cm for the realistic single-sided setup. When studying an anthropomorphic paediatric head phantom both single- and double-sided set-ups performed similarly where the difference in water equivalent thickness (WET) between the two set-ups were less than 0.01 mm in homogeneous areas of the head. Larger discrepancies between the two set-ups were visible in high density gradients like the facial structures. A complete CT reconstruction of a Catphan® module was performed. Assuming ideal detectors, the obtained spatial resolution was 5.1 lp/cm for double-sided and 3.8 lp/cm for the single-sided setup. Double- and single-sided pRad with realistic tracker properties returned a spatial resolution of 3.8 lp/cm and 3.2 lp/cm, respectively. Future studies should investigate the development of dedicated reconstruction algorithms targeted for single-sided particle imaging.
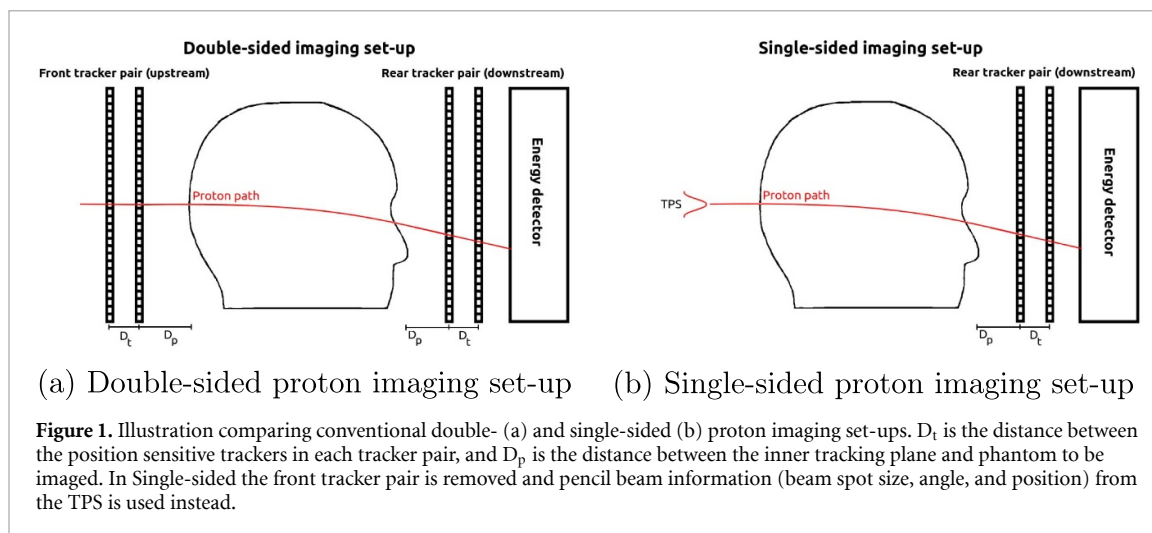
1. Introduction

List-mode proton imaging, where individual protons are detected one-by-one, has gained increasing interest over the recent years as a promising candidate for improving range accuracy in particle therapy treatment planning (Poludniowski *et al* 2015, Hansen *et al* 2015, Dedes *et al* 2019). The main advantage of proton imaging over conventional x-ray imaging modalities is the more accurate determination of the patient's relative stopping power (RSP) from either particle computed tomography (pCT) (Hansen *et al* 2015, Dedes *et al* 2019) or combining a small number of particle radiographs with a treatment planning x-ray CT (Schneider *et al* 2005, Collins-Fekete *et al* 2017b, Krah *et al* 2019). A strong necessity in list-mode proton imaging is an accurate estimation of each proton's trajectory through the object in order to improve the spatial resolution deteriorated by multiple Coulomb scattering (MCS). An accurate estimate of the trajectory of each particle enables a more accurate distribution of the proton energy loss information, improving spatial resolution of reconstructed images (Li *et al* 2006). Several different path estimation methods have been developed, of which the most widely used is the probabilistic most likely path (MLP) formalism that takes advantage of the Fermi-Eyges approximation of MCS (Schneider and Pedroni 1994, Williams 2004, Schulte *et al* 2008, Erdelyi 2009, Collins-Fekete *et al* 2017c, Krah *et al* 2018). The MLP is usually computed from four input parameters—the particle's position and direction at the object entrance and exit. In practice, these parameters are obtained by integrating a set of position sensitive detector planes upstream (front tracker set) and downstream (rear tracker set) the object to be imaged (Poludniowski *et al* 2015). Such a proton imaging set-up (in this work denoted double-sided) is illustrated in figure 1(a).

The accuracy of the MLP depends on the amount of scattering inside the patient, spatial uncertainty of the tracking detectors and their distance to the patient (Krah *et al* 2018). However, for clinical implementation, a system that does not include a front tracker set (here denoted single-sided and illustrated in figure 1(b)) might be more advantageous due to the reduced set-up complexity and reduced cost of the system. Additionally, for proton list-mode imaging at synchrotron facilities, a system using both front and rear trackers might be less practical for acquiring list-mode data at high particle rates: at a synchrotron, the beam typically is delivered in bunches lasting 20 to 50 ns spaced 100 to 200 ns apart (Krimmer *et al* 2018). With increasing average particle rates, the probability of more than one particle being delivered per bunch increases and, hence, the effective particle rate impinging on the detector becomes much larger than the average rate set in the beam control. For list-mode particle imaging, the system would have to be either fast enough to assign a time stamp to every incident particle at the effective rate of the particles within each bunch, or measure a large multiplicity of particles simultaneously as for example proposed in (Pettersen *et al* 2019a). However, measuring a large multiplicity of particles in the same read-out frame compromises the feasibility of including a front tracker to the system, as the MCS in the object makes it difficult to accurately pair particle histories measured on the rear tracker with the measurements on the front tracker. Thus it is of interest to explore the possibility of using a single-sided set-up to avoid this pairing of particle histories. As has been shown by Krah *et al* (2018) for active scanning beam delivery systems, the available treatment planning system (TPS) information (beam spot position/direction as well as spot size and beam divergence) can be included in the derivation of the MLP. From their work it follows that the spatial resolution achievable with a single-sided set-up is limited compared to a double-sided set-up[1]. However, their work focused on the accuracy of the MLP without reconstructed images.

The purpose of this work is hence to investigate the image quality of proton radiography (pRad) and proton CT (pCT) with a single-sided imaging system using Monte Carlo simulations. We assessed the effect of different pencil beam spot sizes and different lateral spacing between pencil beam spot center positions. A 200 mm thick water phantom with aluminium inserts at different depths was imaged to study the spatial resolution with respect to the MLP accuracy and object depth for reconstructed images from single- and double-sided set-ups. For comparing single-sided and double-sided imaging set-ups in a more clinically relevant scenario, pRad of a paediatric head phantom (Giacometti *et al* 2017b) was performed. For investigating and comparing the spatial resolution between single- and double-sided set-ups in pCT, scans of a Catphan® (the Phantom Laboratories, Salem, NY, USA) CTP528 (Line-pair) module was simulated and reconstructed. To investigate the image quality achievable with a single-sided setup in the ideal case, we first used ideal tracking planes having zero material budget and zero pixel pitch. In addition, we compared the results to those acquired with a realistic tracking system modeled after the current state-of-the-art prototype developed by the US pCT collaboration (Johnson *et al* 2017). This study was done in the context of the Bergen pCT project, which is designed to work with clinical pencil beam scanning and a rear tracker set only, and whose detector components are currently under construction.

---

[1]While in their work, Krah *et al* (2018) do not directly investigate a single-sided set-up where the rear tracker also measures the particle direction, it is straightforward to apply their methodology to such a case as well.

Figure 1. Illustration comparing conventional double- (a) and single-sided (b) proton imaging set-ups. D_t is the distance between the position sensitive trackers in each tracker pair, and D_p is the distance between the inner tracking plane and phantom to be imaged. In Single-sided the front tracker pair is removed and pencil beam information (beam spot size, angle, and position) from the TPS is used instead.

2. Materials and methods

2.1. Monte Carlo simulations

All pRad and pCT data were simulated using the Geant4-wrapping GATE V8.2 Monte Carlo toolkit (Jan *et al* 2004, Jan *et al* 2011, Agostinelli *et al* 2003, Allison *et al* 2006). The reference physics list QGSP_BIC_EMZ, as recommended by the GATE Radiation Therapy and Dosimetry working group, was activated for the simulations and the ionization potential of water was manually set to 78 eV. The simulation world was filled with air and default step limits (1 mm) and production cuts (0.7 mm) were used in all simulations.

The tracker planes were implemented as ideal detector planes with zero material budget. For both the double-sided and the single-sided set-ups the distance between the inner tracking plane(s) of the tracker pair(s) to the phantom edge was set to 150 mm and the distance between tracking planes in each set was set to be 50 mm as based on the results from Krah *et al* (2018) and Bopp *et al* (2014). For studying the impact of tracker properties, a realistic tracking system was modeled after the Loma Linda prototype pCT scanner (Giacometti *et al* 2017a, Johnson *et al* 2016). The realistic tracking system comprises four 0.4 mm thick silicon strip detectors (SSD) each with a strip-pitch of 0.228 mm. Two tracker planes are used to form the front and rear tracker sets respectively, with positioning of the trackers equivalent to that for the ideal setup. The proton residual energy was scored directly on the rear tracker and no residual energy uncertainty was modeled, this was done in order to limit the amount of image noise and focus solely on the effect of removing the front tracker pair.

To model a pencil beam scanning system, the GATE built-in treatment plan system (TPS) (Grevillot *et al* 2011) was used. The pencil beam lateral full width at half maximum (FWHM) at the iso-centre was set to 7 mm to represent a clinically realistic beam. Additionally, 2 and 3 mm FWHM spot sizes were investigated. The initial beam energy was set to 230 MeV, representing the highest clinically available beam energy for most contemporary proton therapy facilities. The pencil beam characteristics underlying the investigations presented in this work are detailed in table 1. Field sizes chosen to cover each investigated phantom in pRad were $3.0 \times 3.0 \, \text{cm}^2$ for the spot-phantom, $4.2 \times 4.2 \, \text{cm}^2$ for the step-phantom, and $20 \times 20 \text{cm}^2$ for the head-phantom. A total number of 2×10^6 protons were used to image the step-phantom and 12×10^6 protons to image the head-phantom. Proton CT scans were acquired from 360 projections separated by steps of 1° and containing 1×10^6 primary protons in each projection covering a $16.0 \times 5.0 \, \text{cm}^2$ field consisting of 705 beam spots with a spot FWHM of 7 mm and lateral spot spacing of 3.5 mm.

2.2. Phantoms

Five different phantom geometries were implemented in GATE to investigate the image quality for a single-sided imaging set-up combined with pencil beam scanning.

First, a water tank of 200 mm thickness was implemented to study the behaviour and quality of the MLP compared to the actual MC ground truth path.

The second phantom was a water tank of 200 mm thickness containing a $20 \times 20 \times 20 \, \text{mm}^3$ aluminium cube placed in the water tank's centre. This was used to study the impact of spot-spacing and beam spot size on the spatial resolution of the reconstructed pRad. This phantom will be referred to as "spot-phantom" in this work.

Table 1. TPS set-up and 2, 3, and 7 mm FWHM pencil beam characteristics used to investigate image quality.

TPS source characteristics			
Energy	230 MeV		
Nozzle exit to iso-centre distance	500 mm		
Scanning magnet X to iso-centre distance	6600 mm		
Scanning magnet Y to iso-centre distance	6600 mm		
Beam characteristics	2 mm	3 mm	7 mm
Spot size in x (standard deviation) [mm]	0.85	1.3	3.0
Spot size in y (standard deviation) [mm]	0.85	1.3	3.0
Spot divergence theta [mrad]	2.4	2.8	2.8
Spot divergence phi [mrad]	2.4	2.8	2.8
Spot emittance theta [mm*mrad]	1.1	3.0	3.0
Spot emittance phi [mm*mrad]	1.1	3.0	3.0

(a) Side-view of the step-phantom.

(b) Front/beam-view of the step-phantom.

Figure 2. Side (a) and front view (b) of the step-phantom. Five aluminium cubes of 10 mm edge length were slanted five degrees and placed at different depths in a water tank. The red arrow represents the beam direction and black arrows mark the distances between the centres of the aluminium inserts.
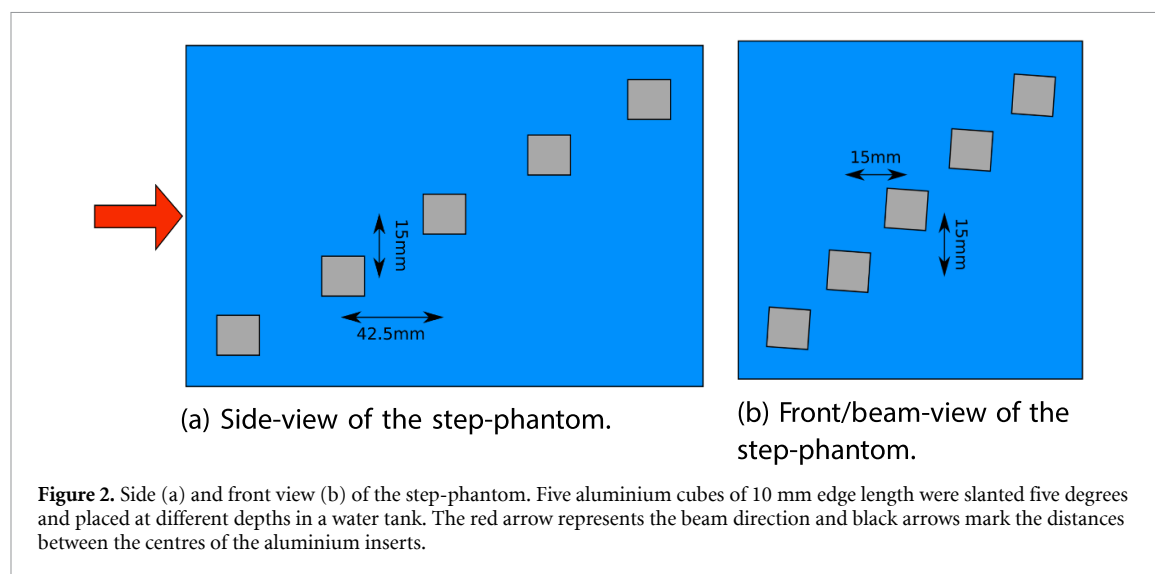
The third phantom investigated was a water tank of 200 mm thickness where five $10 \times 10 \times 10$ mm^3 aluminium cubes were placed at five different depths inside (15 mm, 57.5 mm, 100 mm, 142.5 mm, 185 mm). This phantom is depicted in figure 2 and will be referred to as ''step-phantom'' throughout this work. The cubes were slanted 5 degrees relative to the vertical image pixel direction to enable the evaluation of the modulation transfer function (MTF) from the edge spread of the cubes. This phantom enables the investigation of the spatial resolution as a function of object depth.

To represent a clinically relevant case, a digitised paediatric head phantom based on the CIRS model HN715 (Norfolk, Virginia, USA) was implemented in the simulations. The head is a high resolution ($0.187\,5 \times 0.187\,5 \times 1.25$ mm^3) voxelised geometry developed by Giacometti *et al* (2017b). A ground truth pRad was reconstructed by integrating over the known RSP of every voxel of the head phantom and is used in evaluating radiography reconstruction errors.

The fifth and final phantom was a Catphan® CTP528 (line-pair) phantom module with the purpose of investigating the spatial resolution of a full proton CT scan. The phantom is an epoxy cylinder that contains small aluminium inserts at a fixed radial position with increasing spatial frequency (1–21 line pairs per cm—lp/cm). The phantom was implemented following the specifications in Piersimoni *et al* (2018).

All phantoms were placed such that their center aligned with the iso-centre of the TPS. A complete list of all used material compositions, densities as well as their reference relative stopping power (RSP) can be found in table 2.

2.3. Spot-spacing and spot size

A smaller pencil beam lateral uncertainty and spread is expected to increase the spatial resolution following Krah *et al* (2018). Hence, two pencil beam thicknesses of 7 and 3 mm FWHM were investigated. Smaller spacing in-between spots was also investigated following the rational that for the reconstruction algorithm from Collins-Fekete *et al* (2016) the water equivalent thickness (WET) of each pixel is calculated as a

Table 2. Hounsfield unit (HU), atomic composition (fraction of mass in %), density and RSP of materials used in Monte Carlo simulations.

Material name	HU	H	C	N	O	Mg	Al	Si	Cl	Ca	P	S	Ba	Ar	ρ [g/cm³]	RSP
Air	−998	-	0.01	75.53	23.18	-	-	-	-	-	-	-	-	1.28	0.001204	0.00 114 657
Water	-	11.20	-	-	88.80	-	-	-	-	-	-	-	-	-	1.00	1
Aluminium	-	-	-	-	-	-	100.0	-	-	-	-	-	-	-	2.7	2.12522
Silicon	-	-	-	-	-	-	-	100.0	-	-	-	-	-	-	2.33	1.88521
Epoxy	-	7.8	71.09	2.03	19.08	-	-	-	-	-	-	-	-	-	1.16	1.14341
Soft tissue	24	8.48	57.45	1.65	24.6	7.62	-	-	0.19	-	-	-	-	-	1.055	1.04063
Brain tissue	52	8.17	53.62	1.53	26.51	9.98	-	-	0.19	-	-	-	-	-	1.07	1.04918
Spinal disk	92	7.07	52.46	2.11	27.60	9.55	-	-	0.21	0.98	-	-	-	-	1.10	1.0631
Trabecular bone	197	8.39	59.65	1.55	21.42	1.46	-	-	0.12	5.03	2.33	-	-	-	1.13	1.11113
Cortical bone	923	4.13	29.70	0.85	34.12	3.11	-	-	0.04	20.48	7.57	-	- -	-	1.75	1.59127
Tooth dentin	1280	4.51	35.35	1.23	29.41	-	-	-	0.04	19.84	9.20	0.08	0.33	-	1.66	1.51866
Tooth enamel	2310	2.77	21.81	0.82	34.02	-	-	-	0.03	26.6	12.33	0.31	1.31	-	2.04	1.7955

weighted mean over all protons crossing into the pixel column through the object. Hence, a denser packing of protons corresponding to the center of the beam spot might increase the image accuracy. The spot spacing was set to 0.5 and 1 times the beam lateral FWHM of each beam. Additionally, for the 7 mm beam, a spot spacing of 1 mm was investigated.

2.4. Image reconstruction

In this work, the extended MLP formalism developed by Krah *et al* (2018) was employed to estimate the proton trajectory throughout the phantoms. In this formalism, the TPS parameters (mean beam position and beam direction) were used, and the uncertainty of these parameters were accounted for by including the beam co-variance matrix following section 2.6 in their work. The beam co-variance was obtained at the same position as the innermost front tracker plane in the corresponding double-sided set-up. A hull projection algorithm was applied to project the proton positions from the trackers along their directions and onto the phantom contour positions. This effectively improves the accuracy of the MLP and reconstruction as reported by Schultze *et al* (2015) and Collins-Fekete *et al* (2017a). The WET crossed by each proton was computed by integrating over the inverse stopping power in water ($(dE/dx)_w$) as

$$\text{WET} = \int_{E_{\text{in}}}^{E_{\text{out}}} \frac{1}{(dE/dx)_w} dE. \tag{1}$$

The required list of stopping power versus energy, via data tables covering the proton energy range of 1 to 330 MeV in steps of 0.01 MeV, was obtained directly from MC simulation. Before image reconstruction a $2.5\,\sigma$ filter on the proton angles was applied to filter out the large angle scattering not described by the scattering theory underlying the MLP (Schulte *et al* 2008, Gottschalk 2012). A $3\,\sigma$ filter on the WET of the protons was applied to remove unusually large energy losses and nuclear interactions (Schulte *et al* 2005).

Radiography image reconstruction was performed using the maximum likelihood image reconstruction method developed by Collins-Fekete *et al* (2016). This algorithm offers a reconstructed pRad where the WET of each image pixel is calculated as a weighted mean over all protons crossing into pixel columns through the object. The pixel size for reconstructed pRad was 0.25×0.25 mm^2, except for the anthropomorphic head phantom where it was 0.1875×1.25 mm^2 to coincide with the digitised CT voxels of the phantom.

For pCT reconstructions we used the diagonally-relaxed orthogonal row projection (DROP) iterative reconstruction algorithm with superiorization of the total variation (TVS) (Penfold *et al* 2010). As starting point for the iterative reconstruction and for obtaining the object hull, an analytical CT reconstruction based on the Feldkamp-David-Kress (FDK) algorithm was used. For computational efficiency, an optimised cubic spline path (Collins-Fekete *et al* 2015) was used to interpolate between the particle entrance position/direction estimated from the extended MLP algorithm and the measured rear tracker information, following the work by (Pettersen *et al* 2019b). This approximates the full extended MLP while retaining the computational advantages of the fast cubic spline path. The DROP-TVS algorithm was run for 8 iterations each divided into 40 optimization blocks. The slice thickness was set to 1.25 mm and 455x455 pixels per slice (160 mm radius FOV; 0.35 mm pixel size) were set for the reconstruction.

2.5. Image metrics

The main difference between single-sided and double-sided imaging set-ups is the degradation of the MLP accuracy due to the missing set of front trackers (Krah *et al* 2018, Plautz *et al* 2016). This will result in a decrease in the spatial resolution of the acquired images. We compared the spatial resolution of pRad and pCT acquired with single- and double-sided list mode using the MTF. We computed the edge spread function (ESF) for every insert of the step-phantom and fitted them with an error function to suppress noise. The derivative of the fits yielded the line spread functions, and the MTF was finally obtained as their Fourier transform. As a metric for comparison we used the spatial frequency lp/cm at which the MTF drops below the 10% level as has also been done in previous literature (Seco *et al* 2013, Krah *et al* 2018).

For pRad of the step-phantom, the contrast-to-noise ratio (CNR) of the inserts was evaluated using

$$\text{CNR} = \frac{\overline{\text{WET}}_{\text{AlCube}} - \overline{\text{WET}}_{\text{Water}}}{\sqrt{(\sigma_{\text{AlCube}})^2 + (\sigma_{\text{Water}})^2}}. \tag{2}$$

Where $\overline{\text{WET}}_{\text{AlCube}}$ and σ_{AlCube} are the mean and standard deviation, respectively, of WET values in the central area (2.5×2.5 mm^2) of the aluminium insert. $\overline{\text{WET}}_{\text{Water}}$ and σ_{Water} are the mean and standard deviation of the reconstructed WET values of the homogeneous water tank. A total of 100 image pixels were used for calculating each mean and standard deviation.

The WET errors of the reconstructed pRad of the anthropomorphic head phantom were quantified using the difference between the reconstructed WET pRad and the ground truth pRad. Additionally, the noise in

each image pixel was obtained as the standard error of the mean of the weighted WET distribution in that pixel, where the weights were the same ones used in the image reconstruction from the algorithm by Collins-Fekete *et al* (2016).

For the pCT reconstructions of the Catphan® CTP528 line pair module, the visual MTF was assessed from the maximum-to-minimum contrast measured for each set of line pairs relative to the reference contrast. Following (Piersimoni *et al* 2018), a discrete MTF was then obtained from the contrast $C(f)$ between adjacent maxima and minima in a profile over the line pair inserts of the same spatial frequency f (lp/cm).

$$\text{MTF}(f) = \frac{C(f)}{C(0)}, \tag{3}$$

where

$$C(f) = \left\langle \frac{\text{RSP}_{\text{max}} - \text{RSP}_{\text{min}}}{\text{RSP}_{\text{max}} + \text{RSP}_{\text{min}}} \right\rangle \tag{4}$$

For a robust estimate, the contrast was averaged over all pairs of adjacent maxima and minima corresponding to the same spatial frequency. The contrast at $f = 0$ was obtained as using the peak RSP value reconstructed for the 1 lp/cm aluminium insert and the RSP reconstructed for the epoxy material for the ideal double-sided reconstruction.

3. Results
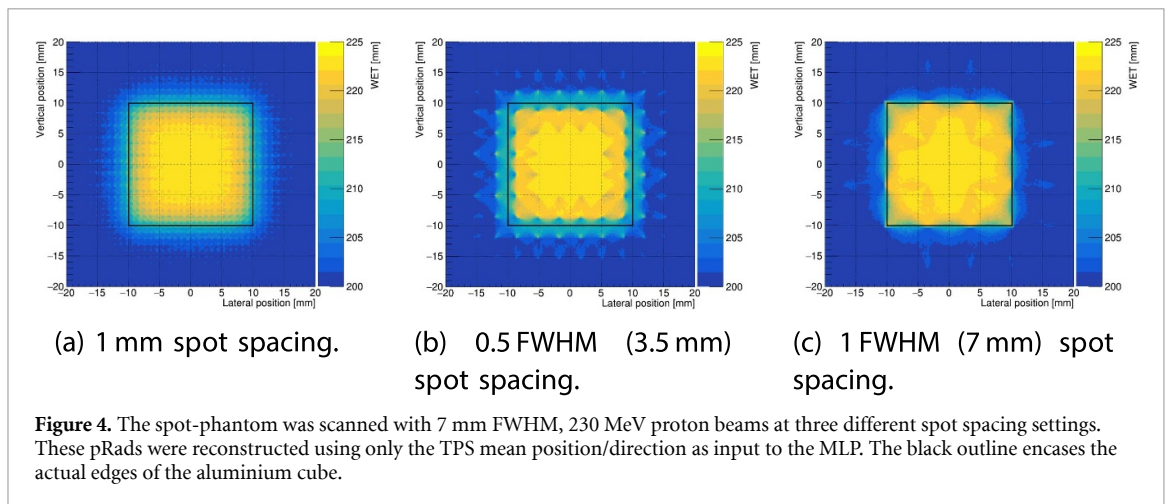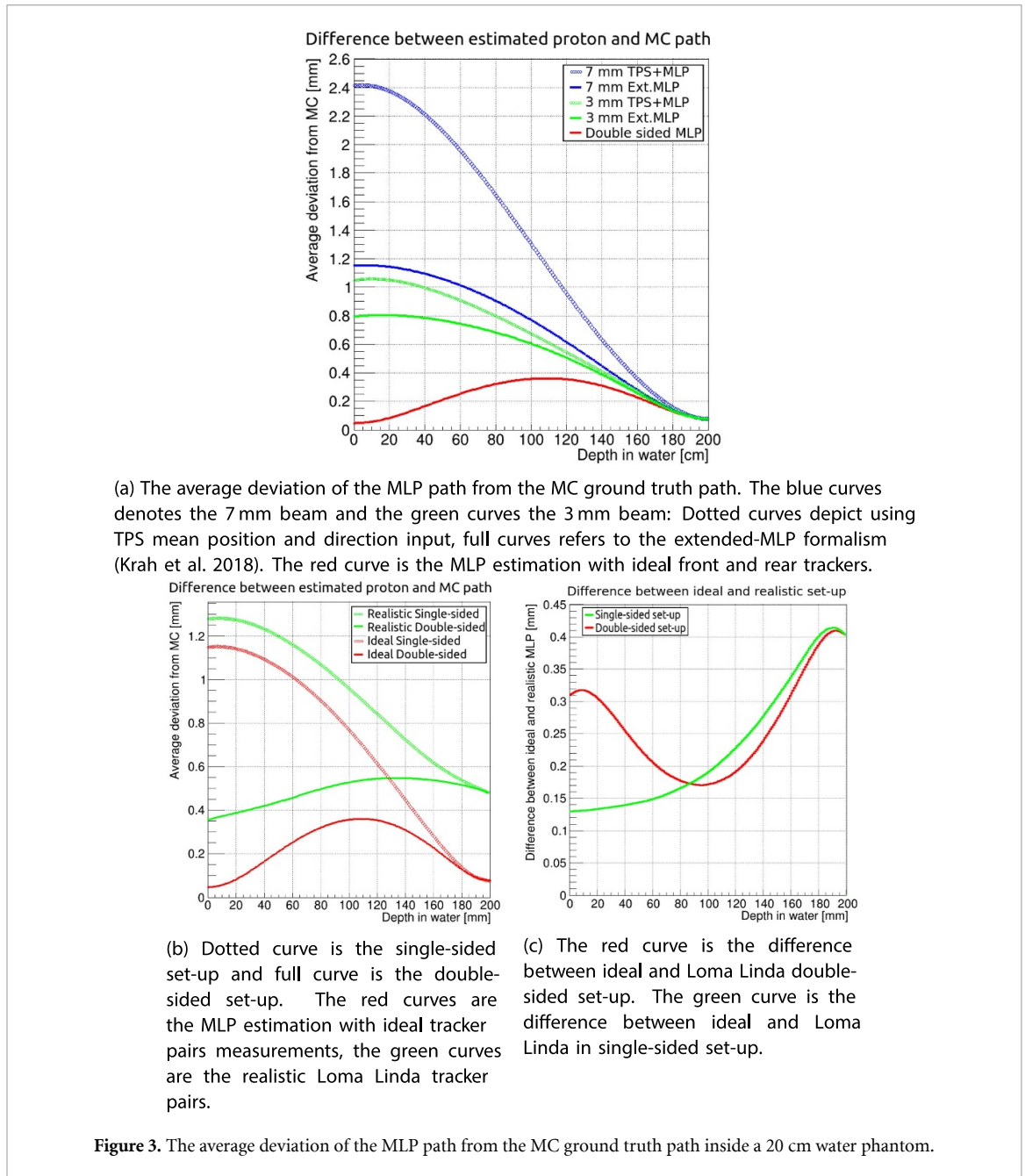
3.1. MLP accuracy impact
The average deviation between the MLP and the MC ground truth path is shown in figure 3(a) as a function of depth in a 200 mm thick water tank for protons with initial energy of 230 MeV. The MLP for the single-sided set-up has the highest deviation in the very beginning of the phantom and continually improves with decreasing distance to the rear trackers. Not taking into account the pencil beam uncertainty and co-variance matrix in the MLP derivation, the MLP deviation is as high as 2.4 mm at the object entrance for a 7 mm FWHM beam. This is improved by a factor 2 when using the extended-MLP formalism by (Krah *et al* 2018). The smaller and more focused 3 mm beam exhibits the same behaviour, albeit with a smaller benefit from the extended-MLP formalism due to the already small width of the incoming pencil beam. However, the single-sided MLP is still less accurate compared to the double-sided set-up. In figure 3(b), the effect realistic tracker properties for setup parameters based on the Loma Linda phase II prototype have on the MLP accuracy is compared to ideal trackers. Due to pixel pitch and scattering inside the trackers, the entrance and exit position accuracy are deteriorated and thus affecting the MLP negatively.

3.2. Spot spacing and spot size
Using only the TPS mean position/direction information as input to the MLP estimation by Schulte *et al* (2008) resulted in considerable image deterioration in the form of sampling artifacts due to the systematic shift in the entrance positions of the particles. This is shown for some selected spot spacing values in figure 4. These artifacts can be understood from figure 5. Using the mean position/direction in the pencil beam as entrance position resulted in a systematic shift of the MLP, particularly in the beginning of the phantom. This resulted in under-sampling of the shaded object regions during image reconstruction with the algorithm by Collins-Fekete *et al* (2016). The size of these empty areas, and therefore the observed sampling artifacts, are dependent on the spot size and similar artifacts were observed for all investigated pencil beam spot sizes and spot spacing. It is noted that a larger amount of proton histories (5×10^6 compared to the original 2×10^6) were used during the image reconstruction of spot-phantom pRad to more clearly visualise the patterns being induced by the image artifacts caused by the spot-spacing.

These artifacts disappear for the 7 mm beam when the initial position of the proton is estimated using the extended-MLP. No difference in spatial resolution nor noise was observed for any of the three investigated spot spacing for the 7 mm beam. For the double-sided set-up, the image quality was not affected by the spot size and the spacing between spots, as expected.

For the smaller 2 mm and 3 mm FWHM spots, however, artifacts were present in the reconstructed single-sided pRad when a 1 FWHM spot spacing was used. This becomes apparent for the step-phantom as seen in figure 6(c). These artifacts stem from the the smaller corresponding uncertainty of the TPS mean position involved in the calculation of the extended-MLP (Krah *et al* 2018): For a highly focused beam, the extended-MLP will effectively approach the pencil beam mean position and underestimate the spread of protons entering the phantom, as observed in figure 6(b) and (d). The underestimated spread induces
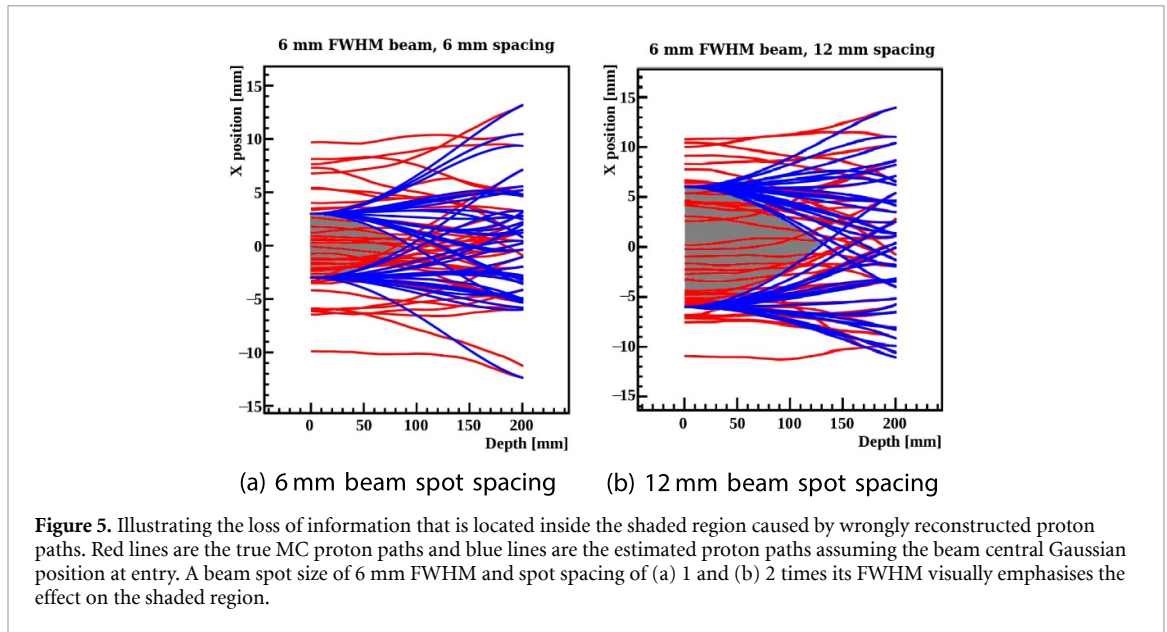
(a) The average deviation of the MLP path from the MC ground truth path. The blue curves denotes the 7 mm beam and the green curves the 3 mm beam: Dotted curves depict using TPS mean position and direction input, full curves refers to the extended-MLP formalism (Krah et al. 2018). The red curve is the MLP estimation with ideal front and rear trackers.

(b) Dotted curve is the single-sided set-up and full curve is the double-sided set-up. The red curves are the MLP estimation with ideal tracker pairs measurements, the green curves are the realistic Loma Linda tracker pairs.

(c) The red curve is the difference between ideal and Loma Linda double-sided set-up. The green curve is the difference between ideal and Loma Linda in single-sided set-up.

Figure 3. The average deviation of the MLP path from the MC ground truth path inside a 20 cm water phantom.

(a) 1 mm spot spacing.

(b) 0.5 FWHM (3.5 mm) spot spacing.

(c) 1 FWHM (7 mm) spot spacing.

Figure 4. The spot-phantom was scanned with 7 mm FWHM, 230 MeV proton beams at three different spot spacing settings. These pRads were reconstructed using only the TPS mean position/direction as input to the MLP. The black outline encases the actual edges of the aluminium cube.

(a) 6 mm beam spot spacing   (b) 12 mm beam spot spacing

Figure 5. Illustrating the loss of information that is located inside the shaded region caused by wrongly reconstructed proton paths. Red lines are the true MC proton paths and blue lines are the estimated proton paths assuming the beam central Gaussian position at entry. A beam spot size of 6 mm FWHM and spot spacing of (a) 1 and (b) 2 times its FWHM visually emphasises the effect on the shaded region.

Table 3. $MTF_{10\%}$ at five different depths inside a 200 mm thick water tank for both ideal and realistic single- and double-sided imaging set-ups. For each cube the corresponding CNR is given in parentheses.

Depth [mm]	Double-sided Ideal [lp/cm]	Single-sided Ideal [lp/cm]	Double-sided Realistic [lp/cm]	Single-sided Realistic [lp/cm]
15	7.2 (13.5)	2.6 (13.6)	4.7 (12.8)	2.4 (14.6)
57.5	5.9 (13.8)	2.7 (12.9)	4.7 (13.5)	2.4 (14.0)
100	4.8 (12.3)	3.1 (11.6)	4.1 (14.5)	3.0 (14.0)
142.5	3.6 (13.7)	3.7 (13.4)	3.5 (13.1)	3.0 (13.4)
185	2.9 (13.0)	2.9 (12.4)	2.9 (11.3)	2.5 (12.8)

similar artifacts as in figure 4 which can be mitigated by a smaller spot spacing due to the overlapping of the proton distributions and preventing loss of information in gaps between pencil beam spots. For the 7 mm FWHM beam, the estimated pencil beam entrance distribution from the extended-MLP approaches the true distribution of the protons as shown in figure 6(f).
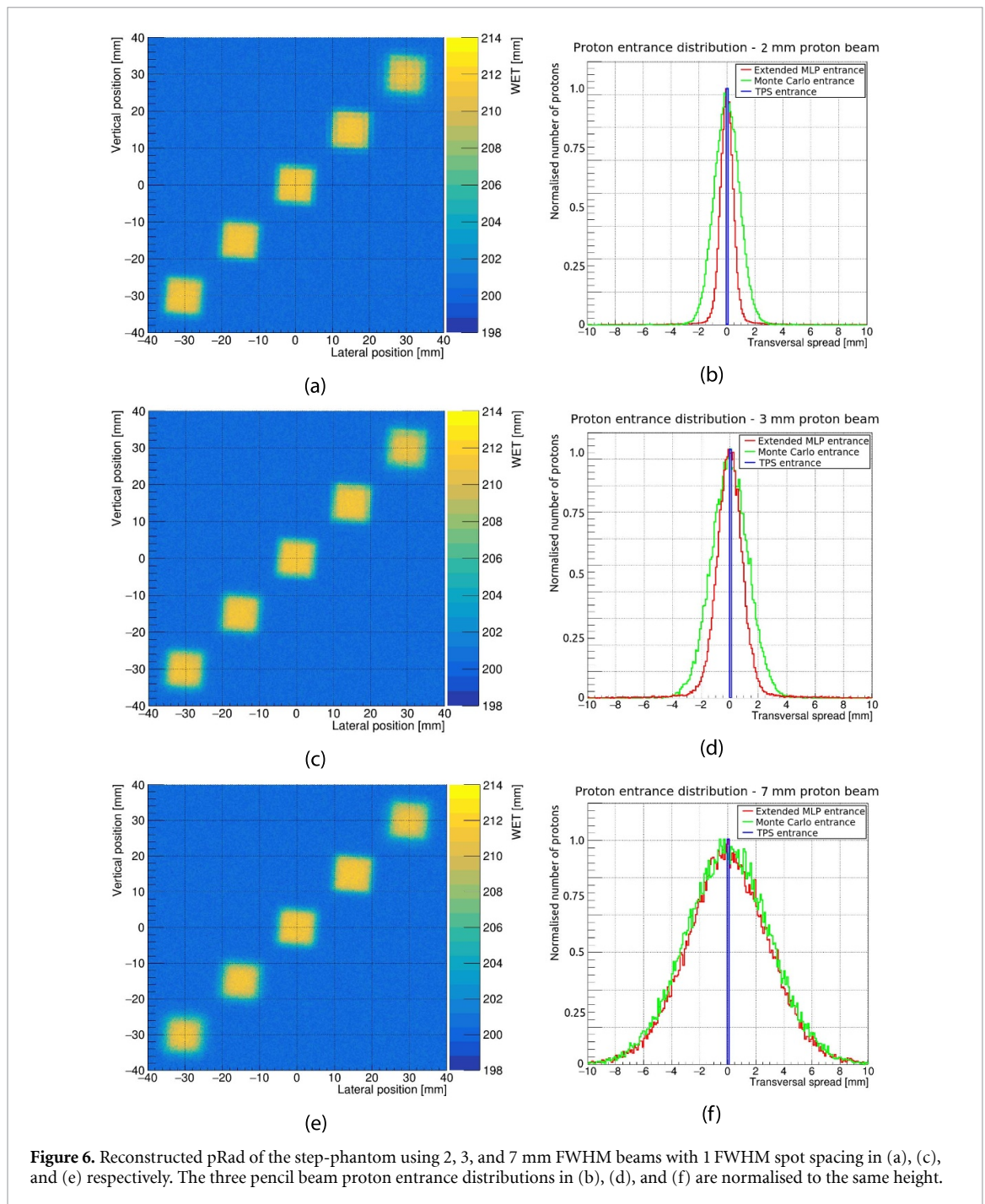
3.3. Spatial resolution

The step-phantom was irradiated with the 7 mm pencil beam and 0.5 FWHM spot spacing to evaluate the spatial resolution achievable with a clinically realistic beam. The $MTF_{10\%}$ together with their contrast-to-noise ratio (CNR) for each of the five aluminium inserts are presented in table 3. The average resolution of the edges of the five cubes of the reconstructed step-phantom pRad in figure 7 are 4.9 lp/cm for the double-sided set-up and 3.0 lp/cm for the single-sided set-up. For the realistic tracker set-ups the average resolution is 4.0 lp/cm for double-sided set-up and 2.7 lp/cm for single-sided.

3.4. Radiography of the paediatric head phantom

To investigate a clinically relevant scenario, the 7 mm and 3 mm beam with 0.5 FWHM spot spacing were used to image an anthropomorphic paediatric head phantom. The reconstructed WET from both the double- and single-sided pRad are compared to the ground truth integrated WET image in figure 8. WET error profiles through different parts of the phantom are shown in figures 8(c)–(e) for easier comparison of double- and single-sided set-ups. Figure 9 shows the equivalent for reconstructions based on realistic tracker properties.

In figures 8(a) and (b), the single-sided pRad resulted in higher errors at high WET gradients, especially around the facial features like the nose cavity and mouth. Profiles through the homogeneous part of the brain (figure 8(c), between lateral position -40–40 mm) yielded a WET error for both set-ups that is better than 1% of the total WET in that region, while the facial structures in figures 8(d) and (e) have WET errors between 1% and up to 3%. The average difference in reconstructed WET between double-sided and single-sided imaging in the homogeneous area of the brain was less than 0.01 mm. At high density gradient structures around the mouth, the difference between the two set-ups can reach over 1 mm. Similar results

Figure 6. Reconstructed pRad of the step-phantom using 2, 3, and 7 mm FWHM beams with 1 FWHM spot spacing in (a), (c), and (e) respectively. The three pencil beam proton entrance distributions in (b), (d), and (f) are normalised to the same height.

were observed in pRad with realistic trackers, albeit yielding larger errors at high WET gradients, reaching up to 5% of the WET in the facial structures. The difference between single- and double-sided set-ups in these regions was also larger, reaching up to 2 mm difference. This increased error originates from the more impaired MLP of realistic tracker properties. In homogeneous areas however, such as the brain, there is little to no difference between the imaging set-ups.

To quantify the image noise in both single- and double-sided pRad, the standard deviation of the reconstructed WET in each image pixel is shown in figure 10, where the top row shows the ideal, and the bottom row the realistic tracker setup. Again, the single-sided reconstruction shows elevated noise levels compared to the double sided one at high WET gradients.

3.5. Spatial resolution of pCT
Figure 11 shows a central slice through the double-sided and single-sided pCT reconstructions of the Catphan® CTP528 line pair module. The single-sided pCT shows a reduced spatial resolution compared to

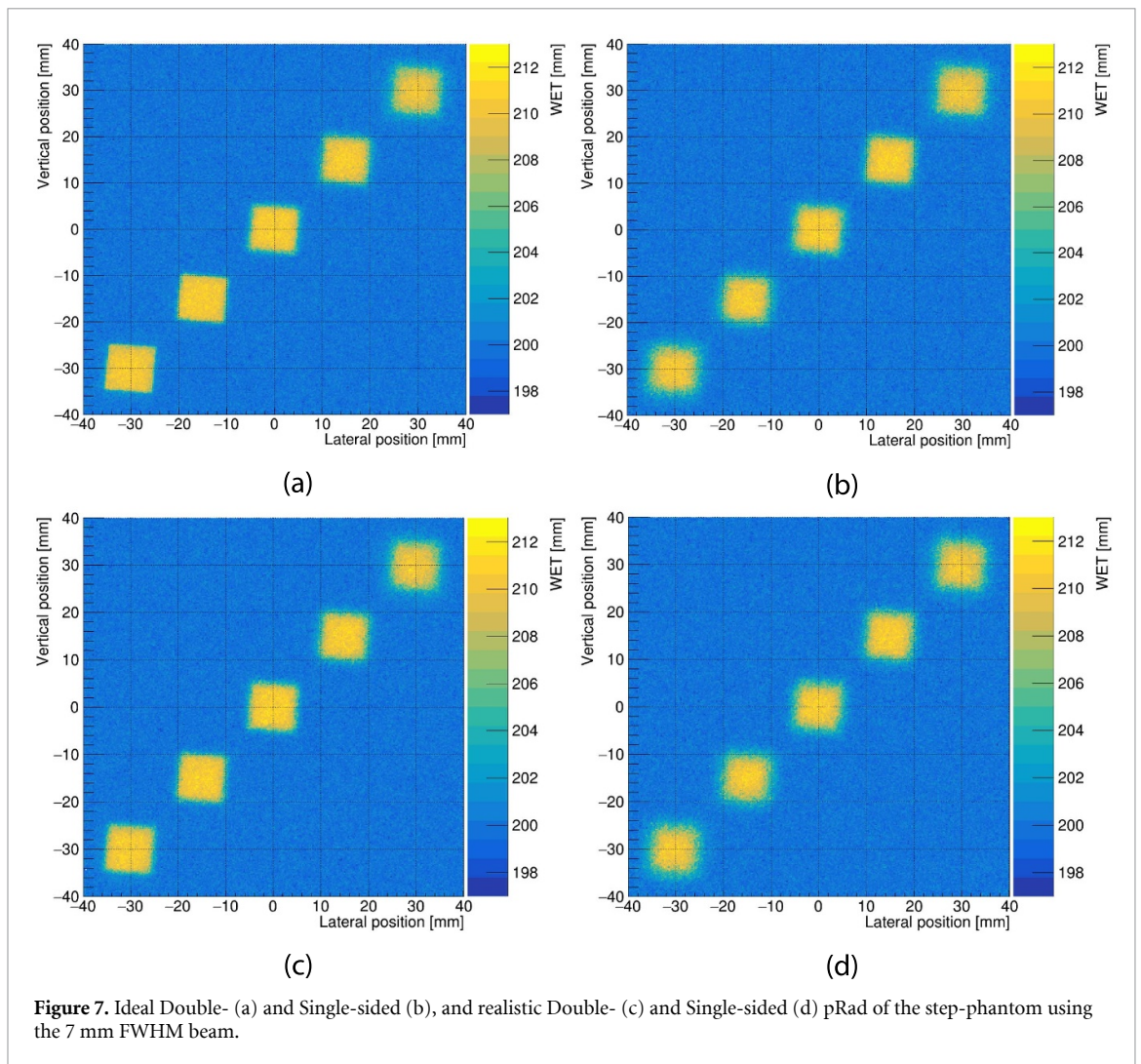**Figure 7.** Ideal Double- (a) and Single-sided (b), and realistic Double- (c) and Single-sided (d) pRad of the step-phantom using the 7 mm FWHM beam.
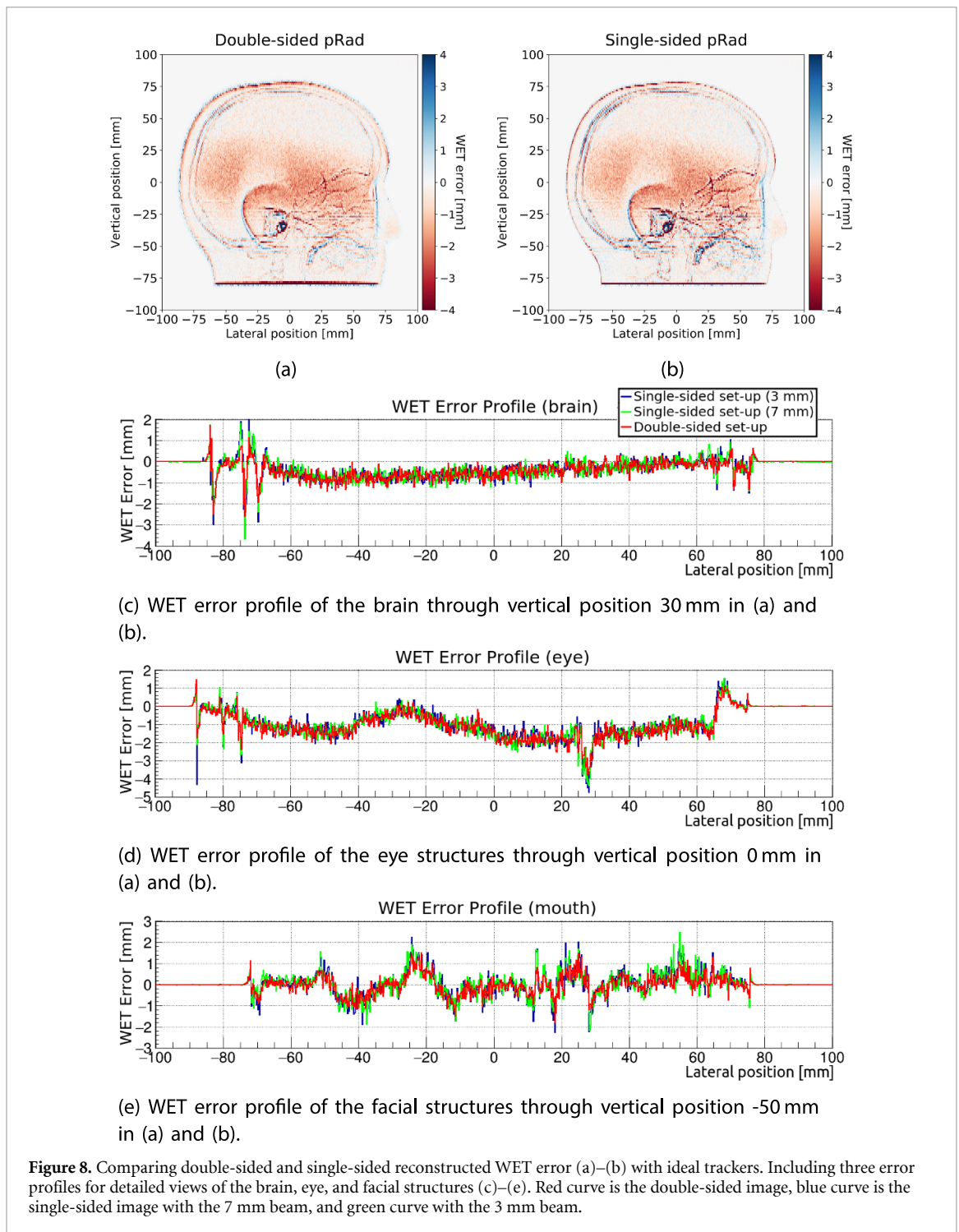
the double-sided one. Figure 12 shows the $\text{MTF}_{10\%}$ computed from the maximum-to-minimum contrast for each set of line pairs relative to the reference contrast.

Overall, the MTF of double-sided pCT was above that of the single-sided reconstructions. For an ideal imaging setup, single-sided pCT had a $\text{MTF}_{10\%}$ of 3.8 lp/cm while that for double-sided pCT was 5.1 lp/cm. When realistic tracker properties were used in simulating the projection data, the $\text{MTF}_{10\%}$ was 3.2 lp/cm for the single-sided setup, while it was 3.9 lp/cm for the double sided setup.
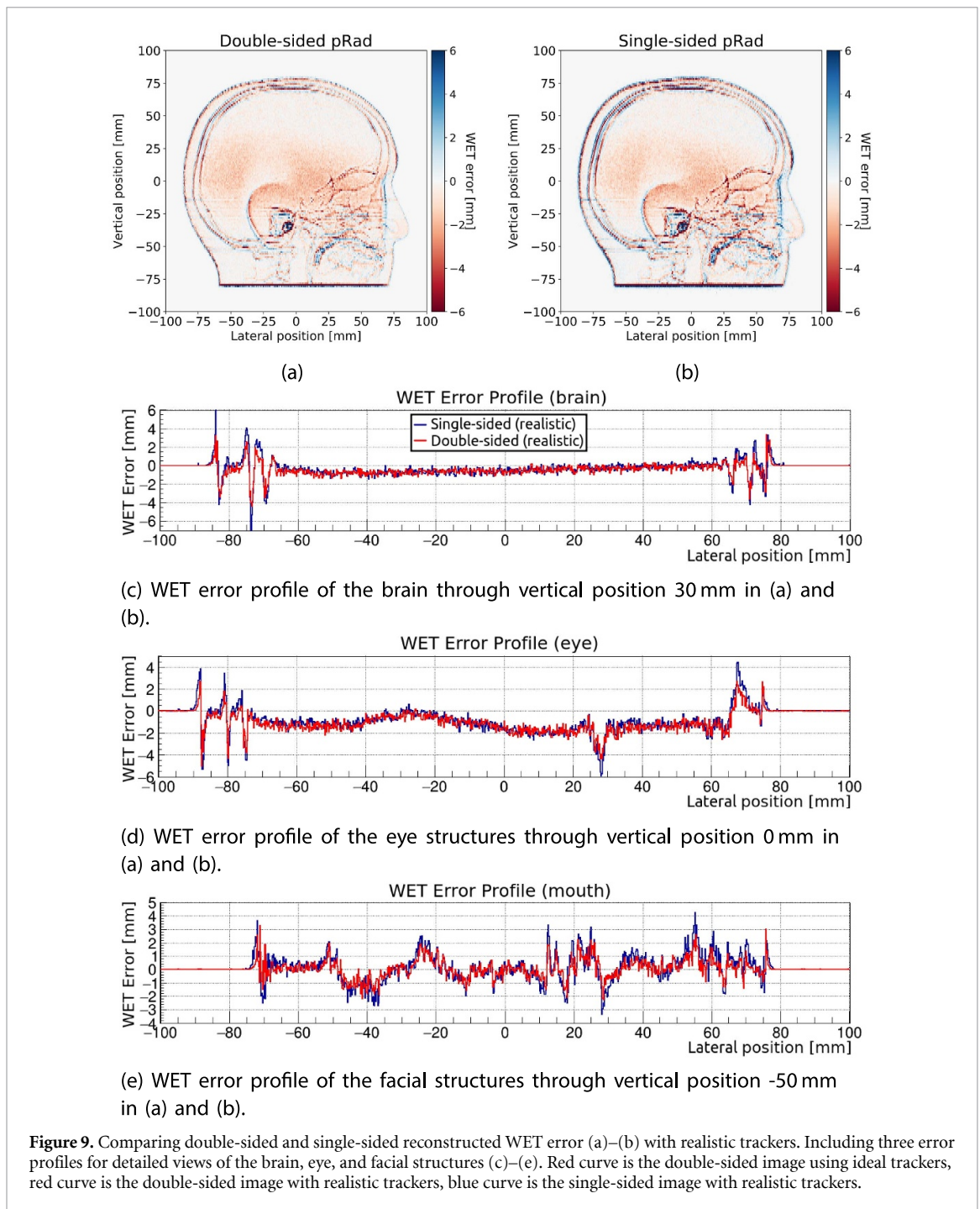
4. Discussion

4.1. Choice of set-up parameters

In this work, we investigated the image quality achievable with a single-sided proton imaging set-up compared to a double-sided set-up. To this end, we focused our work on clinically realistic beam parameters, and also studied the effect of varying the spot spacing and pencil beam size. In order to demonstrate the potentially achievable image quality for single-sided imaging, an ideal imaging system was implemented. This enables us to draw conclusions on the feasibility of single-sided imaging independent of the specific detector design and material budget. However, as shown already in Bopp *et al* (2014) and Krah *et al* (2018), a realistic tracking system deteriorates the MLP accuracy. Hence, in order to investigate the feasibility of single-sided imaging based on currently available technology, a realistic imaging system was modeled after the prototype pCT detector system developed by the US pCT collaboration. As expected, these realistic tracker properties had a negative effect on the MLP accuracy of both single- and double-sided setups (figure 3). For the double-sided setup, a larger decrease in MLP accuracy was observed at the entrance region compared to the single-sided setup (see figure 3(b)). This is not surprising, as for the 200 mm water tank investigated, the uncertainty on the rear tracker measurement projected onto the phantom entrance is dominated by the scattering and therefore less influenced by the introduction of tracker uncertainties

Figure 8. Comparing double-sided and single-sided reconstructed WET error (a)–(b) with ideal trackers. Including three error profiles for detailed views of the brain, eye, and facial structures (c)–(e). Red curve is the double-sided image, blue curve is the single-sided image with the 7 mm beam, and green curve with the 3 mm beam.

compared to the double-sided setup. Position sensitive detectors with lower material budget or smaller pixel pitch as envisioned in the design of the Bergen pCT system (Pettersen *et al* 2019a) would improve the image quality for both single-and double-sided reconstructions towards the ideal case (Krah *et al* 2018). It has to be noted that although realistic position trackers are included in the analysis, no realistic energy detection is included as this would only serve to increase the total image noise compared to what is shown in figures 10(a)–(d) (see Dickmann *et al* (2019) for an extensive investigation of the different noise sources of a realistic detector set-up).
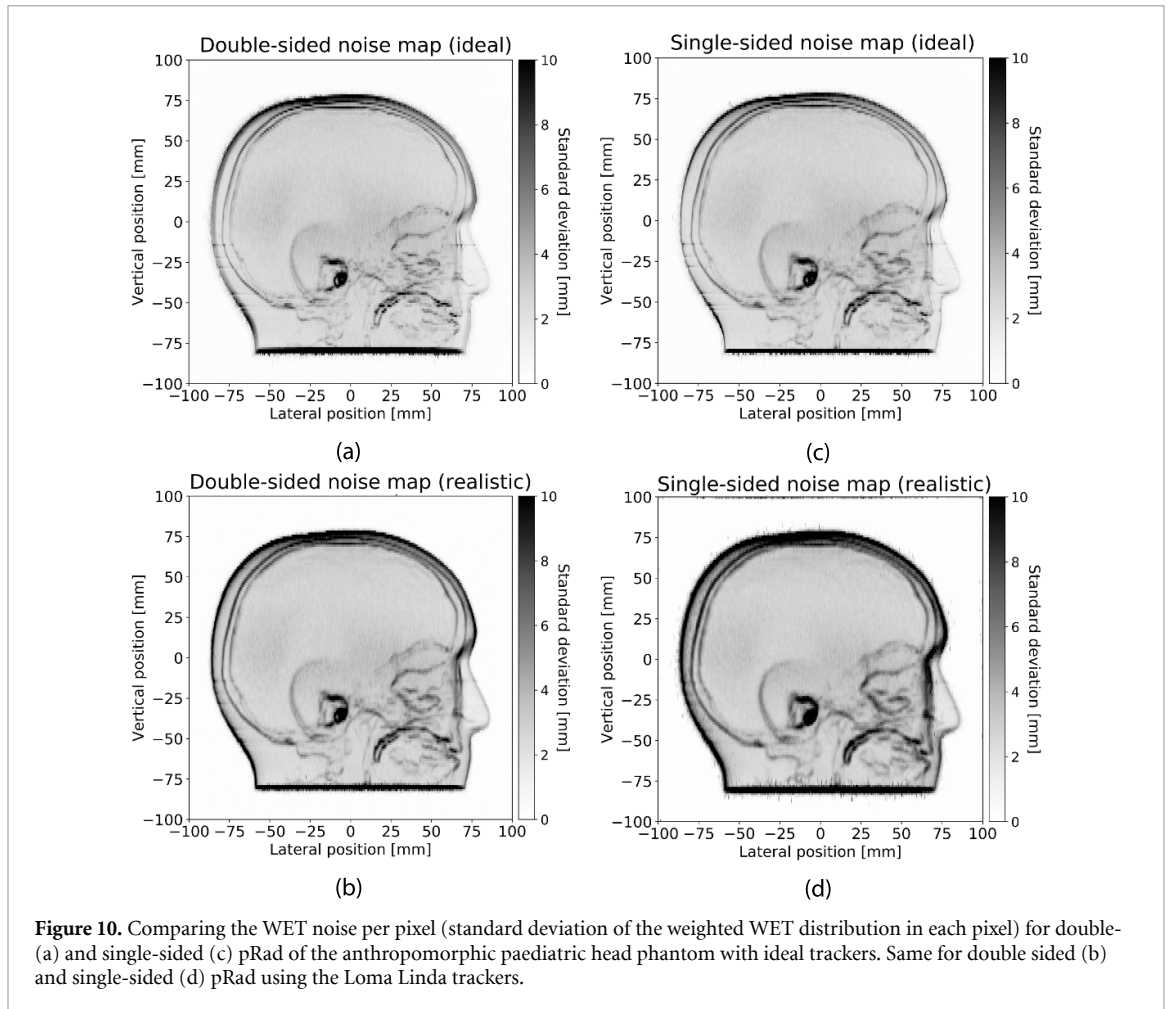
A beam energy of 230 MeV was chosen, representing the highest energy setting commonly available at contemporary proton therapy facilities. A higher beam energy would improve the path estimation quality and the overall spatial resolution of the acquired images. However, for energy detection in particle imaging, where the beam is required to stop within the energy detector, choosing a higher beam energy would require a larger energy detector and hence, setting an arbitrarily high energy would not represent a clinically realistic

Figure 9. Comparing double-sided and single-sided reconstructed WET error (a)–(b) with realistic trackers. Including three error profiles for detailed views of the brain, eye, and facial structures (c)–(e). Red curve is the double-sided image using ideal trackers, red curve is the double-sided image with realistic trackers, blue curve is the single-sided image with realistic trackers.

case. In addition, with increasing energy, the noise due to range straggling would also increase (Collins-Fekete *et al* 2020). On the other hand, choosing a lower beam energy than the one investigated here would lead to increased scattering and hence negatively affect the path estimation. Especially for single-sided imaging, the increased scattering would reduce the confidence in the remaining tracker information. In turn, the path estimation would depend more on the TPS information which can lead to systematic artifacts (see discussion below). It is also noted, that lowering the initial energy would cause an increase in the image noise due to the multiple Coulomb scattering (Collins-Fekete *et al* 2020).

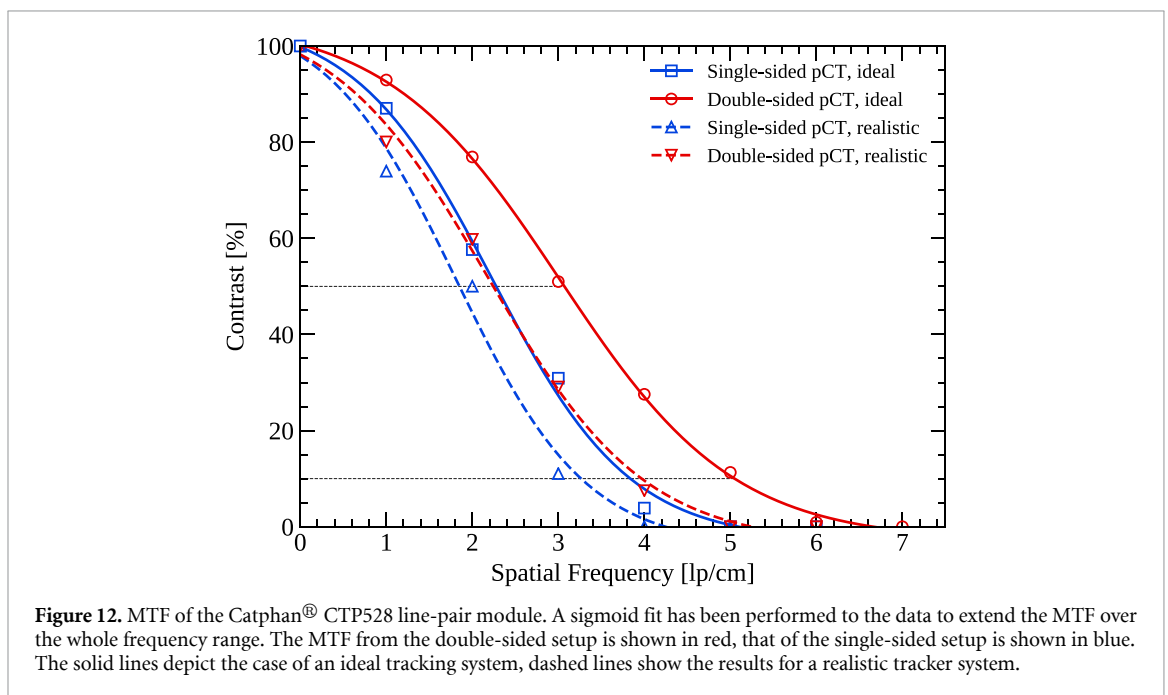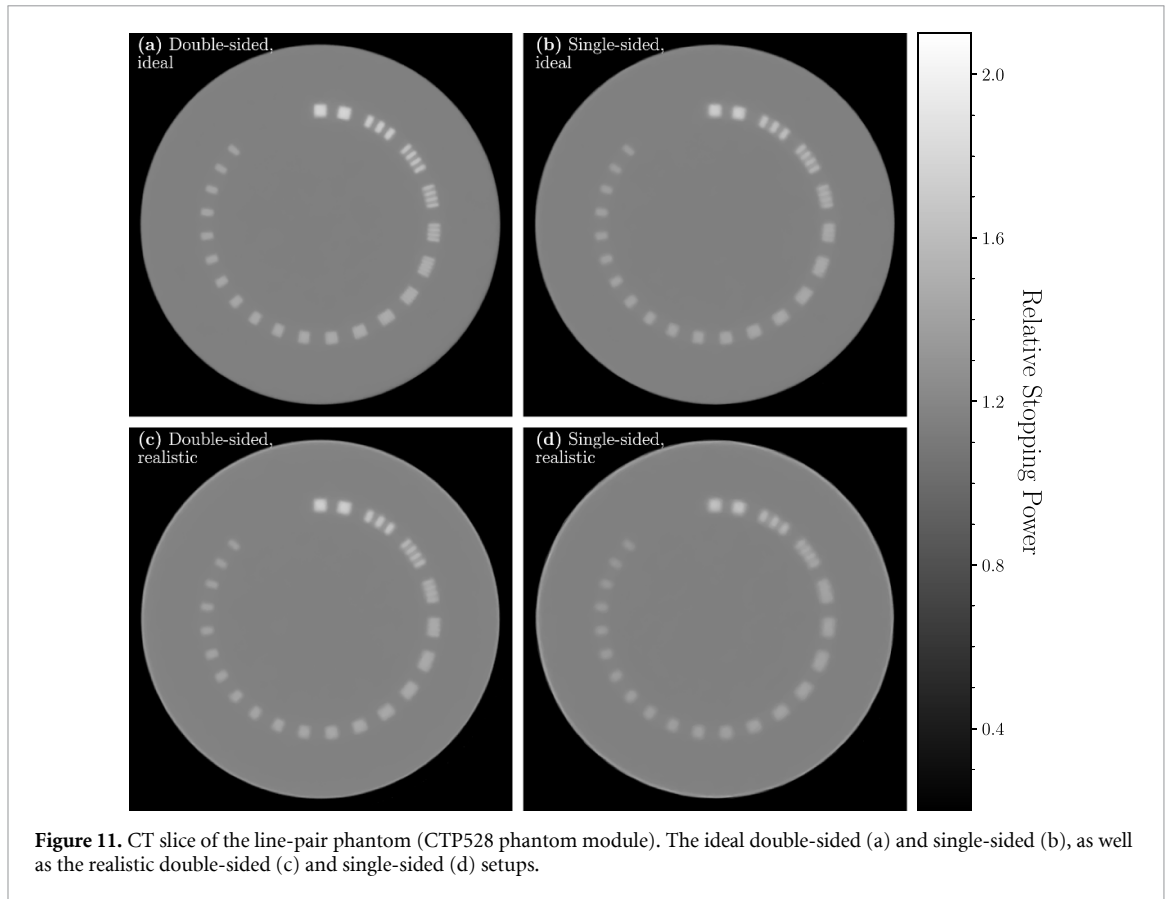## 4.2. Image quality of single-sided proton imaging

Overall, the achievable image quality of single-sided proton imaging using contemporary image reconstruction techniques was lower compared to that of double-sided proton imaging, as expected. For pRad with ideal tracker planes, an average spatial resolution of 3.0 lp/cm was observed for single-sided pRad in contrast to the 4.9 lp/cm for double-sided pRad evaluated using a sharp edge gradient technique on the step-phantom inserts. For the reconstructions using realistic trackers, the spatial resolution decreased by

Figure 10. Comparing the WET noise per pixel (standard deviation of the weighted WET distribution in each pixel) for double-(a) and single-sided (c) pRad of the anthropomorphic paediatric head phantom with ideal trackers. Same for double sided (b) and single-sided (d) pRad using the Loma Linda trackers.

18% to 4.0 lp/cm for the double-sided setup, whereas it only decreased by 10% for the single-sided setup averaging at 2.7 lp/cm. For the single-sided setups, the spatial resolution was particularly deteriorated for the aluminium cubes located close to the entrance region when compared to the double-sided image, due to the lower path estimation quality in that region. It is also noteworthy that for both imaging set-ups, a decrease in spatial resolution was observed for the aluminium cubes close to the object exit, and that the spatial resolution constantly decreased with increasing depth for the double-sided pRad. This behavior of the spatial resolution with depth for the double-sided set-up is in contrast to the expected behavior when looking at the uncertainty of the MLP as a function of depth in figure 3(a). However, it is in-line with the observations made in the experimental work by Gehrke *et al* (2018). This is connected to the maximum likelihood radiography reconstruction method and will be detailed in a further study to be brought forward by our group.

The pencil beam spot size as well as the distance between spots was varied to study the effect of these parameters on the image quality. In the double-sided imaging set-up, since every single proton position is measured both before and after the phantom, no adverse nor beneficial effect of smaller spot spacing or smaller FWHM pencil beam sizes was observed nor expected, given that the applied fluence field amply covers the phantom. For single-sided imaging, all pencil beam sizes and lateral distances between spots induced sampling artifacts in the reconstructed images if only the pencil beam mean position/direction from the TPS was used as input to the path estimation. These were attributed to the systematic error in the proton entrance position and hence, systematic errors in the calculation of the weighted mean for each image pixel in the algorithm by Collins-Fekete *et al* (2016).

When using the extended-MLP formalism by Krah *et al* (2018) no spot spacing artifacts were observed for the 7 mm FWHM beam. However, the increased MLP accuracy associated with a thin pencil beam (2 and 3 mm FWHM) did not manifest as expected in the image quality. Instead, for the more focused 2 and 3 mm beam spot sizes the extended-MLP algorithm underestimated the spread of proton entrance positions, as can be seen in figures 6(b) and (d). This resulted in sampling artifacts in the reconstructed pRad of the step-phantom similar to the ones observed when only the TPS mean position was used as input to the MLP estimation. For the two investigated beam widths, these artifacts could be removed by using a smaller spot

Figure 11. CT slice of the line-pair phantom (CTP528 phantom module). The ideal double-sided (a) and single-sided (b), as well as the realistic double-sided (c) and single-sided (d) setups.

Figure 12. MTF of the Catphan® CTP528 line-pair module. A sigmoid fit has been performed to the data to extend the MTF over the whole frequency range. The MTF from the double-sided setup is shown in red, that of the single-sided setup is shown in blue. The solid lines depict the case of an ideal tracking system, dashed lines show the results for a realistic tracker system.

spacing covering up the loss of information between the spots. The reason for these artifacts resides within the calculation of the MLP from Krah *et al* (2018): The more certain the information provided by the pencil beam is compared to that of the rear tracker propagated to the object entrance, the less the rear tracker measurement will contribute to the estimation of the MLP at the entrance position. Hence, the entrance point of the protons will be systematically shifted closer to the TPS mean position/direction. Particularly, this depends on the rear tracker properties as well as on the scattering inside the object—and with that on the beam energy, object thickness and object material. In that regard, artifacts observed for the step-phantom were not observed for the anthropomorphic paediatric head phantom scanned with the 3 mm FWHM pencil

beam, likely due to the lower WET of the phantom. To get the best possible image quality in single-sided list-mode proton imaging, the pencil beam size could be optimised as function of beam and set-up parameters in future investigations. It is important to note that a decreasing spot size and spot distance in the plan the minimum dose required to deliver the plan increases, depending on the minimum time required to irradiate a treatment spot (order of 1 ms (Schoemers *et al* 2015)).

For the paediatric head phantom investigated, the lower spatial resolution of single-sided pRad can be seen at the facial structures in the form of an increased WET error (figure 7(b)) and increased pixel noise (figure 10(c)) compared to double-sided reconstruction. Since the objective of taking a pRad for particle therapy would be pre-treatment patient alignment as well as potentially pre-treatment optimization of the Hounsfield Unit to relative stopping power lookup table (HLUT) (Collins-Fekete *et al* 2017b, Krah *et al* 2019), the impact of the lower spatial resolution in that context would need to be investigated. Especially for the optimization of the HLUT from the method by Collins-Fekete *et al* (2017b), a reduced performance of the single-sided set-up would be expected due to the reduced path estimation accuracy. However, the WET error and noise for the homogeneous regions of the head phantom were comparable for both single-sided and double-sided set-ups, albeit the realistic tracker properties increased the difference between the setups at heterogeneous regions. Since for the optimization of the HLUT, a smaller image area can be used (Krah *et al* 2019), the feasibility of single-sided proton imaging for pre-treatment optimization would need to be systematically evaluated before definitive conclusions can be drawn.

For the simulated pCT of the CTP528 line pair module, the MTF was evaluated for both single-sided and double-sided set-ups acquired with the 7 mm FWHM scanned beam as above. With ideal trackers, the $MTF_{10\%}$ was 3.8 lp/cm for single-sided compared to 5.1 lp/cm for the double-sided pCT reconstruction, i.e. reduced by ~25%. For realistic trackers, the difference between the two setups was 18%, with $MTF_{10\%}$ of 3.2 lp/cm and 3.9 lp/mm for single- and double-sided setups, respectively. It has been argued in the work of Krah *et al* (2018) that due to typical commercial TPS voxel size of 2 mm, the image resolution from pCT imaging should be no worse than 3 lp/cm to enable treatment planning. Following this argumentation, the single-sided set-up, in the realistic case, returned a spatial resolution just at the limit for clinical usefulness. Hence, future work should carefully investigate whether treatment planning with a single-sided pCT system would indeed be feasible.

Possible improvements of the spatial resolution of single-sided proton imaging set-ups are currently being investigated in our group. Especially, choosing helium ions to generate the images would improve the achievable image quality, due to the helium ions' reduced MCS compared to that of protons (Hansen *et al* 2014, Collins-Fekete *et al* 2017c, Volz *et al* 2017, Gehrke *et al* 2018, Piersimoni *et al* 2018). Future work will include the development of optimised image reconstruction techniques, targeted specifically for single-sided proton imaging.

5. Conclusion

In this work, we have compared single-sided and double-sided proton list-mode imaging. As expected, leaving out the front tracker and using the pencil beam information to reconstruct the protons paths during image reconstruction reduced the spatial resolution and increased the image noise. Using only the TPS mean position as input in conventional MLP estimation induced significant image artifacts and was ruled out for single-sided proton imaging. As of writing, the extended-MLP by Krah *et al* (2018) is thus the only viable MLP estimation algorithm for use in single-sided proton imaging. When investigating the impact of the pencil beam properties on the image quality, we observed that by using the extended-MLP formalism, a smaller pencil beam spot size introduced sampling artifacts to the reconstructed image. This was shown to result from a systematic bias in the estimation of the proton paths towards the pencil beam spot's mean position. Since this shift in the estimated proton path is subject to the uncertainty of the rear tracker measurements as well as to the scattering of the protons inside the phantom, the optimal beam spot size and spot spacing should be evaluated as function of the detection system and object properties. Single-sided pCT with a realistic rear tracker pair resulted in a spatial resolution just above what is suggested for accurate treatment planning. In future studies, the usefulness of single-sided pCT for treatment planning should to be carefully investigated based on different patient sites.

ORCID iDs

Jarle Rambo Sølie ⓘ https://orcid.org/0000-0002-8327-8248
Lennart Volz ⓘ https://orcid.org/0000-0003-0441-4350
Helge Egil Seime Pettersen ⓘ https://orcid.org/0000-0003-4879-771X
Pierluigi Piersimoni ⓘ https://orcid.org/0000-0002-8958-2179
Håvard Helstrup ⓘ https://orcid.org/0000-0002-9335-9076
Ilker Meric ⓘ https://orcid.org/0000-0001-5659-3907

References

Agostinelli S, Allison J, Amako K, Apostolakis J, Araujo H *et al* 2003 Geant4—a simulation toolkit *Nucl. Instrum. Methods Phys. Res.* A **506** 250–303

Allison J, Amako K, Apostolakis J, Araujo H, Dubois P A *et al* 2006 Geant4 developments and applications *IEEE Trans. Nucl. Sci.* **53** 270–8

Bopp C, Rescigno R, Rousseau M and Brasse D 2014 The impact of tracking system properties on the most likely path estimation in proton CT *Phys. Med. Biol.* **59** N197–N210

Collins-Fekete C-A, Bär E, Volz L, Bouchard H, Beaulieu L and Seco J 2017a Extension of the Fermi-Eyges most-likely path in heterogeneous medium with prior knowledge information *Phys. Med. Biol.* **62** 9207–19

Collins-Fekete C-A, Brousmiche S, Hansen D C, Beaulieu L and Seco J 2017b Pre-treatment patient-specific stopping power by combining list-mode proton radiography and x-ray CT *Phys. Med. Biol.* **62** 6836

Collins-Fekete C-A, Brousmiche S, Portillo S K N, Beaulieu L and Seco J 2016 A maximum likelihood method for high resolution proton radiography/proton CT *Phys. Med. Biol.* **61** 8232

Collins-Fekete C-A, Dikaios N, Royle G J and Evans P M 2020 Statistical limitations in proton imaging *Phys. Med. Biol.* **65** 085011

Collins-Fekete C-A, Doolan P, Dias M F, Beaulieu L and Seco J 2015 Developing a phenomenological model of the proton trajectory within a heterogeneous medium required for proton imaging *Phys. Med. Biol.* **60** 5071–82

Collins-Fekete C-A, Volz L, Portillo S K N, Beaulieu L and Seco J 2017c A theoretical framework to predict the most likely ion path in particle imaging *Phys. Med. Biol.* **62** 1777

Dedes G, Dickmann J, Niepel K B, Wesp P, Johnson R P *et al* 2019 Experimental comparison of proton CT and dual energy X–ray CT for relative stopping power estimation in proton therapy *Phys. Med. Biol.* **64** 165002

Dickmann J, Wesp P, Rädler M, Rit S, Pankuch M, Johnson R P, Bashkirov V, Parodi K, Landry G and Dedes G 2019 Prediction of image noise contributions in proton computed tomography and comparison to measurements *Phys. Med. Biol.* **64** 145016

Erdelyi B 2009 A comprehensive study of the most likely path formalism for proton-computed tomography *Phys. Med. Biol.* **54** 6095–122

Gehrke T, Amato C, Berke S and Martišíková M 2018 Theoretical and experimental comparison of proton and helium-beam radiography using silicon pixel detectors *Phys. Med. Biol.* **63** 035037

Giacometti V, Bashkirov V A, Piersimoni P, Guatelli S, Plautz T E *et al* 2017a Software platform for simulation of a prototype proton CT scanner *Med. Phys.* **44** 1002–16

Giacometti V, Guatelli S, Bazalova-Carter M, Rosenfeld A B and Schulte R W 2017b Development of a high resolution voxelised head phantom for medical physics applications, *Phys. Med.* **33** 182–8

Gottschalk B 2012 Techniques of proton radiotherapy: transport theory (arXiv:1204.4470)

Grevillot L, Bertrand D, Dessy F, Freud N and Sarrut D 2011 A Monte Carlo pencil beam scanning model for proton treatment plan simulation using GATE/GEANT4 *Phys. Med. Biol.* **56** 5203–19

Hansen D C, Bassler N, Sørensen T S and Seco J 2014 The image quality of ion computed tomography at clinical imaging dose levels *Med. Phys.* **41** 111908

Hansen D C, Seco J, Sørensen T S, Petersen J B B, Wildberger J E, Verhaegen F and Landry G 2015 A simulation study on proton computed tomography (CT)stopping power accuracy using dual energy CT scans as benchmark *Acta Oncol.* **54** 1638–42

Jan S *et al* 2011 Gate v6: a major enhancement of the GATE simulation platform enabling modelling of CT and radiotherapy *Phys. Med. Biol.* **56** 881

Jan S, Santin G, Strul D, Staelens S and Assié K *et al* 2004 GATE: a simulation toolkit for PET and SPECT *Phys. Med. Biol.* **49** 4543–61

Johnson R P *et al* 2017 Results from a prototype proton-CT head scanner *Physics Procedia* **90** 209–14

Johnson R P, Bashkirov V, DeWitt L, Giacometti V and Hurley R F *et al* 2016 A fast experimental scanner for proton CT: Technical performance and first experience with phantom scans *IEEE Trans. Nucl. Sci.* **63** 52–60

Krah N, Khellaf F, Létang J M, Rit S and Rinaldi I 2018 A comprehensive theoretical comparison of proton imaging set-ups in terms of spatial resolution *Phys. Med. Biol.* **63** 135013

Krah N, Patera V, Rit S, Schiavi A and Rinaldi I 2019 Regularised patient-specific stopping power calibration for proton therapy planning based on proton radiographic images *Phys. Med. Biol.* **64** 065008

Krimmer J, Dauvergne D, Letang J and Testa E 2018 Prompt-gamma monitoring in hadrontherapy: A review *Nucl. Instrum. Methods Phys. Res.* A **878** 58–73

Li T, Liang Z, Singanallur J V, Satogata T J, Williams D C and Schulte R W 2006 Reconstruction for proton computed tomography by tracing proton trajectories: A Monte Carlo study *Med. Phys.* **33** 699

Penfold S N, Schulte R W, Censor Y and Rosenfeld A B 2010 Total variation superiorization schemes in proton computed tomography image reconstruction *Med. Phys.* **37** 5887–95

Pettersen H E S, Alme J, Barnaföldi G G, Barthel R and van den Brink A *et al* 2019a Design optimization of a pixel-based range telescope for proton computed tomography *Phys. Medica: European J. Med. Phys.* **63** 87–97

Pettersen H, Volz L, Sølie J, Röhrich D and Seco J 2019b Estimating a proton's position in a pencil beam for proton imaging *Poster session presented at the Conf. of PTCOG*

Piersimoni P, Faddegon B A, Méndez J R, Schulte R W, Volz L and Seco J 2018 Helium CT: Monte Carlo simulation results for an ideal source and detector with comparison to proton CT *Med. Phys.* **45** 3264–74

Plautz T E, Bashkirov V, Giacometti V, Hurley R F, Johnson R P, Piersimoni P, Sadrozinski H F-W, Schulte R W and Zatserklyaniy A 2016 An evaluation of spatial resolution of a prototype proton CT scanner *Med. Phys.* **43** 6291–300

Poludniowski G, Allinson N M and Evans P M 2015 Proton radiography and tomography with application to proton therapy *Br. J. Radiol.* **88** 20150134

Schneider U and Pedroni E 1994 Multiple Coulomb scattering and spatial resolution in proton radiography *Med. Phys.* **21** 1657–63

Schneider U, Pemler P, Besserer J, Pedroni E, Lomax A and Kaser-Hotz B 2005 Patient specific optimization of the relation between CT-Hounsfield units and proton stopping power with proton radiography *Med. Phys.* **32** 195

Schoemers C, Feldmeier E, Naumann J, Panse R, Peters A and Haberer T 2015 The intensity feedback system at Heidelberg Ion-Beam Therapy Centre *Nucl. Instrum. Methods Phys. Res.* A **795** 92–9

Schulte R W, Bashkirov V, Klock M C L, Li T, Wroe A J, Evseev I, Williams D C and Satogata T 2005 Density resolution of proton computed tomography *Med. Phys.* **32** 1035–46

Schulte R W, Penfold S N, Tafas J T and Schubert K E 2008 A maximum likelihood proton path formalism for application in proton computed tomography *Med. Phys.* **35** 4849–56

Schultze B, Witt M, Censor Y, Schubert K and Schulte R 2015 Performance of hull-detection algorithms for proton computed tomography reconstruction *Infinite Products of Operators and Their Applications, of Contemporary Mathematics* eds Reich S and Zaslavski A (Providence, RI: American Mathematical Society) pp 636

Seco J, Oumano M, Depauw N, Dias M F, Teixeira R P and Spadea M F 2013 Characterizing the modulation transfer function (MTF) of proton/carbon radiography using Monte Carlo simulations *Med. Phys.* **40** 091717

Volz L, Collins-Fekete C-A, Piersimonii P, Johnson R P, Bashkirov V, Schulte R and Seco J 2017 Stopping power accuracy and spatial resolution of helium ion imaging using a prototype particle CT detector system *Cur. Dir. Biomed. Eng.* **3** 401–4

Williams D C 2004 The most likely path of an energetic charged particle through a uniform medium *Phys. Med. Biol.* **49** 2899